EXPERIMENTAL-CUM-NUMERICAL EVALUATION OF STRUCTURAL PROPERTIES AND VIBRATIONAL SPECTRA OF NEW SMART TWISTING ACTIVE ROTOR BLADES

Se Hoon Chang, Dept. of Aerospace Information Eng., Konkuk University, Seoul, South Korea
Seong Hyun Hong, Dept. of Aerospace Information Eng., Konkuk University, Seoul, South Korea
Sung Nam Jung, School of Mechanical and Aerospace Eng., Konkuk University, Seoul, South Korea
Do-Hyung Kim, Korea Aerospace Research Institute (KARI), Daejeon, South Korea
Franziska Becker, German Aerospace Center (DLR), Braunschweig, Germany
Steffen Kalow, German Aerospace Center (DLR), Braunschweig, Germany
Rinaldo Steininger, University of Glasgow, Glasgow, United Kingdom

Abstract

In this work, the natural vibrational characteristics of STAR (Smart Twisting Active Rotor) II blades are examined to assess the accuracy of the structural properties obtained using the digitally replicated model constructed based on the X-ray CT (Computer Tomography) scan images of the blade. The frequencies measured using various test setups established at German Aerospace Center (DLR) are exploited for the study. The frequency measurements include the blades installed in a hover test rig at non-rotating or rotating condition along with a bench-top test of the blade mounted vertically with clamping at the root. A detailed three-dimensional (3D) finite element (FE) analysis model created using the MSC.NASTRAN is used to verify the present analysis. The comparison results indicate good agreements for the centroidal offsets and non-rotating frequencies of a cantilevered blade with uniform section only. Systematic parameter studies on the structural dynamic aspects of the blades are conducted, which include the anisotropic couplings of composites, structural load paths over the blade arm region, control stiffnesses, external equipment, and flap bending stiffnesses of the blade. The impact of modeling parameters on the free vibration characteristics of the blades are discussed and some important findings are summarized resulting from the present investigation.

1. INTRODUCTION

In general, the helicopters in flight suffer from high vibration and noise despite their superior capability of vertical take-off and landing, and hover performance. A variety of actuation methodologies have been devised to alleviate the problem (Ref. 1). One promising concept is to use piezo ceramic actuators embedded into the structure to twist the blade actively and thereby to control the rotor without relying on mechanical devices. This active twist concept was first demonstrated by the induced strain actuation of distributed piezoceramic actuators (Ref. 2) and later using the piezoelectric macro fiber composites (MFC) by the NASA/Army/MIT team (Refs. 3-4). These earlier studies demonstrated a great potential in realizing the helicopter rotor applications. Then, an international consortium project called STAR was launched (Ref. 5) to exploit the active twist capability in the large low speed facility (LLF) of the German-Dutch wind tunnel (DNW). The wind tunnel test was originally planned in 2013. However, a structural integrity problem coupled with actuator failures during the pre-test run (Ref. 6) led to a suspension of the program. The sources of the failures were later identified resulting in substantial modifications in the blade structures and rearrangements in MFC actuator panels (Ref. 7). These

Copyright Statement

The authors confirm that they, and/or their company or organization, hold copyright on all of the original material included in this paper. The authors also confirm that they have obtained permission, from the copyright holder of any third-party material included in this paper, to publish it as part of their paper. The authors confirm that they give permission, or have obtained permission from the copyright holder of this paper, for the publication and distribution of this paper as part of the ERF proceedings or as individual offprints from the proceedings and for inclusion in a freely accessible web-based repository.

changes cause significant increases in structural weights and stiffnesses of the new STAR II blades, as compared with the initial designs.

Recently, a digitally replicated model of the STAR II blade has been constructed covering the entire span length by the X-ray computer tomography (CT) scan combined with digital image processing technique (Ref. 8). The detailed cross-section layouts and material zones of the inner structure are identified from a color segmentation process, discriminating subregions with identical X-ray attenuation coefficients in the body. The segmented section profiles are then processed to produce graphic data interfaces to create a finite element (FE) model of the designated sections. Finally, a FE-based cross-section analysis program KSAC2D (Refs. 9-10) is used to determine the 2D sectional properties of the blade. This unique method allows evaluating the structural properties without cutting-up a blade while capturing the details of the structural and material inhomogeneity such as the manufacturing imperfections and sensor cable distributions of the blade in the physical domain (Refs. 8,11). The validity of the digital model was confirmed by correlating the predicted blade mass and sectional stiffnesses with the measured data. In the previous studies, however, the measured data were obtained only in static environments. In addition, need is to refine the cross-sectional analysis models while correctly implementing the material properties and composite layer geometries that match with the manufactured configurations of the blade.

In the present work, the natural vibrational characteristics of the STAR II blades is examined to assess the accuracy of the structural properties (stiffnesses, inertia, and section offsets) predicted using the digitally replicated blade model. To this end, the measured frequencies obtained using the rotor test setups at German Aerospace Center (DLR) in Braunschweig, Germany, are investigated. The measurements include the blades installed at a rotor test rig in either non-rotating or rotating condition as well as the blade mounted vertically while clamping at the root. A detailed 3D FE analysis results using the MSC.NASTRAN are correlated to evaluate the accuracy of the present predictions. Systematic parameter investigations are engaged then to identify the importance of various modeling elements on the natural vibration characteristics of STAR II blades. The parameters include: anisotropic couplings of composites; structural load paths of the blade hub; control stiffnesses; external equipment (e.g., terminal box, tip cap); and flap bending stiffnesses of the blade.

2. ANALYSIS METHODOLOGIES

This section describes the essential features of STAR II rotor, the measurement of blade natural frequencies, and the digital reproduction of the blades, followed by the theoretical background of the cross-sectional analysis system KSAC2D.

2.1. STAR Blades

Figure 1 shows a re-fabricated STAR II blade (epsilon) containing all equipment such as the root cable box and the tip cap (Fig. 1(a)), along with an assembled view of the blade and the arm (Fig. 1(b)). The detailed information regarding the structure of the blade and the complex manufacturing process is described in Kalow et al. (Ref. 12). The STAR rotor is a four-bladed, Mach-scaled experimental model of the production BO-105 helicopter. The rotor has a solidity 0.077 with the radius (R) 2 m and the chord (c) 0.121 m. The blades are of rectangular planform with a linear pretwist distribution of -8^{o}/R along the span length. Table 1 summarizes the general properties of STAR II rotor. The general characteristic of the rotor remains nearly identical to its predecessor HART (Ref. 17) and HART II rotors (Ref. 18) except that the STAR II rotor has: (1) clockwise rotor rotation; (2) articulated hinges; (3) on-blade MFC actuator patches installed underneath the blade skin; and (4) much greater volume of sensors and cable accessories equipped inside the blade structure.

Regarding the no. 4 above, more than 200 pressure sensors (mostly positioned at blade outboard stations) and 25 strain gages (9 for flap and torsion; 7 for lag) are installed per the blade. These instrumentation sensors and MFC actuators inevitably accompany a number of copper cables connecting the data terminal and their origins. The cables are counted as many as 524, 68, and 32 for the pressure sensors, strain gauges, and MFC patch actuators, respectively. In contrast, only a small fraction of the sensors are instrumented in HART II blades (51 pressure sensors and 5 strain gages). It should be noted that the same volume of dummy sensors and copper cables are arranged for each blade to maintain the static and dynamic features as closely as possible between the blades. In general, the sensors have negligible influence on the blade responses due to their small weight (e.g, less than 2 g for a pressure sensor). However, the effects of cables can not be neglected considering the number of counts, span length, and the high-density copper material used for cables. These are addressed carefully as will be shown later in the following section.

2.2. Measurement of STAR II Blade Frequencies

The natural vibration characteristics of STAR II blades are evaluated recently using different rotor test setups, with either non-rotating or rotating condition of the rotor. The former includes the blades in a cantilevered or a rigged (hover test) condition. All the measurements were made using the experimental test facilities available in DLR Braunschweig. First, a bench-top laboratory test was conducted to find the fundamental frequencies and their vibrating modes of the STAR II blades while clamping the blade at the root (see Fig. 2(a)). To this end, each blade was mounted vertically using a mechanical vise while exciting the structure by a hammer shock. A few accelerometers were positioned over the blade surface to pick up the vibration signals. A total of eight modes were identified including four flap, two lag, and two torsion modes. The frequency range measured was up to about 120 Hz (close to seven per revolution) and the averaged values between the blades were obtained to represent the blades.

Figure 2(b) shows a STAR II blade in a rotor test rig (with control linkages connected) for measuring the flap modes in non-rotating condition. As can be seen, three accelerometers (each 5.5 g in mass) attached over the blade surface are distributed along the radius, with the application of the vibration shaker near the blade root. To measure the bending modes, a straight bar made of foam was used to support the blade at the estimated node position for specific blade modes. The same sensor arrangements were used for the lag bending modes with the blade hanged by a rope at 70% radial station. In the torsion mode setup (not shown), two accelerometers were attached around the far edges of the blade chord near the tip with the blade supported at the flap hinge.

The natural frequencies of the individual blades in rotating environments were evaluated next in a whirl tower test facility at DLR Braunschweig, as can be seen in Fig. 3. The rotational speed was increased from 200 rpm to the nominal 1,041 rpm with an interval of approximately 100 rpm (10 measurements in total). The two innermost MFC segments were used to excite the blades with swept-sine signals of 400 V amplitude for the desired modes. For instance, both segments were actuated in phase or out of phase to obtain the torsion or flap bending modes, respectively. The resulting blade motions were sensed using the strain gages positioned outboard of the blade. The data was gathered for 40 sec. with the rate of 1,024 samples per the rotor revolution. The individually measured frequencies exhibited substantial deviations between the blades, and hence they were averaged to obtain the mean of the specific modes of the vibration. It should be noted that there was a difficulty in identifying the blade modes because of the substantial coupling between the flap and torsion modes.

2.3. Sectional Segmentation and Discretization

The X-ray CT (Computer Tomography) scan images constructed based on the work of Ahn et al. (Ref. 8) for STAR II epsilon blade are used to generate the 2D cross-sectional analysis models and then evaluate the structural properties. As described in Ref. 8, the blade has been divided into six regions to conduct the CT scans considering the physical limitation of the X-ray test facility. The window of scan per the projection is thus set to be 155 mm in the chord direction, resulting in a resolution of 361 μm per the digital pixel image. This image resolution was shown to be generally adequate in identifying the different material zones in the STAR blade constructions (Ref. 8).

Figure 4 shows the blade drawing superposed upon X-ray scan images of six subregions (denoted as S1 to S-6) corresponding to the blade root, transition, and the uniform airfoil region until the tip. Note that the blade in use for X-ray scan is of pure structural compositions without containing the metal parts (e.g., root cable box unit and tip bracket), mainly to avoid X-ray artifacts that can be generated from materials with high density composition (Ref. 11). In reality, there are many regions with large density materials in STAR blades, such as MFC actuators, sensor cables, and balancing weights. These generally accompany strong artifacts exhibited in the form of line streaks or blurring of domain edges, leading to poor image quality in the end. In order to compensate for the difficulty in identifying the material domains, the original CAD drawings and the detailed fabrication layouts (composite ply layups) are referred throughout to clarify each of the different material zones. In Figure 4, the specific blade stations for 2D sectional analysis (9 sections in total) are indicated as well. They are denoted as R1 to R5 for blade root and transition regions, and U1 to U4 for airfoil blade region. The respective stations are meticulously chosen considering the geometric variations and the material distributions of the blade. It should be noted that most of the airfoil stations contain MFC actuators which aggravate the X-ray image quality due to the reason mentioned earlier. This problem is overcome exploiting the superior image quality of U4 while assuming that the airfoil region has uniform distribution of structural stiffnesses.

In Figure 5, some of the X-ray CT scan images and the corresponding finite element (FE) discretized models are illustrated for the respective sections. As can be seen, the detailed interior layouts as well as the different material zones of the structure are clearly discerned in black and white scale. The darker zones in the X-ray image indicate regions of low-density material with small attenuation coefficients while the brighter zones signifying greater material density. The specific zones inside the blade structure are identified (called segmentation) considering the level of gray scales in the pixel images and the known structural topologies of the blade. Once specific material zones are identified from the color segmentation process, each segmented region is prescribed by discrete surfaces using a preprocessor (MSC.PATRAN). This leads to numerous sub regions with prescribed boundary edges, each having the same material density. The FE modeling and simulation are then engaged to discretize and analyze the corresponding sections of the blade.

Figure 6 represents the section segmentation images of the blade stations R2 and U1, respectively. Each material domain with the same X-ray attenuation coefficient is distinguished in specific color codes. It should be noted that the manufacturing imperfections and material inhomogeneities (e.g., skin thicknesses, resin layers) are captured as they appear in the real fabricated blades. The respective mechanical material properties designated in Fig. 6 can be found in Ahn et al. (Ref 8). The nose weight consists of tungsten, CFRP (Carbon Fiber Reinforced Plastic), and epoxy resin which are distributed in the blade span length while being enclosed by 0.1 mm thickness resin in the section. The smeared material properties of the nose weight are obtained using the rule of mixtures between the participated materials considering the material contents in both the radial and the cross-sectional directions.

As depicted in the X-ray images (Fig. 5), a cluster of sensor cables and MFC actuator wires are installed in the blade. The cables are made of copper-silver with a polytetrafluorethylene (PTFE, Teflon®) coating while gluing them together as a group. They are clustered near the front (pressure cables), mid (strain gage cables), and rear (actuator cables) portions of the section. The influence of sensor cables should be negligible for the blade stiffnesses. However, these affect the sectional mass (CG) and inertia properties considerably due to the volumes (more than 500 counts) and the high-density copper material in use. Since the cables vary substantially along the length, their impact on the structural properties should be taken into account appropriately. To this end, the airfoil region is divided into discrete stations (U1 to U4), considering the non-uniform distribution of instrumented cables along the span, while keeping the stiffnesses remain constant over the MFC domain (U1 to U3). Figure 7 shows the prescribed zones bounded for each cable group. A rule of mixture between the cables, epoxy resin, and foam is used to determine the equivalent material density of each cable group. Then, a mass lumping technique is applied to compute the mass and inertia properties. Once the FE discretizations for all the sections are made, a 2D cross-sectional analysis is carried out to evaluate the structural properties of the blade. The theoretical backgrounds of the cross-section analysis program and the rotating free vibration analysis of a rotor are briefed in the following sections.

2.4. Blade Cross-sectional Analysis

A general purpose, FE-based two-dimensional cross-sectional analysis program KSAC2D (Konkuk Section Analysis Code 2D; Refs. 9, 15) is employed to analyze the individual cross sections discretized for the blade (see Figure 5). The KSAC2D is an expanded version of the previous Ksec2d (Ref. 16) that can analyze generic beams and blades with arbitrary sectional geometries and material distributions. The validity of the program has been demonstrated at the Korean helicopter development program (Ref. 17) and the evaluation of HART II blade properties (Refs. 11, 14). While the earlier version is equivalent to the Euler-Bernoulli for bending and St. Venant for torsion, the latest KSAC2D has the level of Timoshenko for bending and shear, and Vlasov for torsion, leading to (7×7) stiffness coefficients. Some essential features of the theory are given below.

The formulation is established based on the displacement-based anisotropic elasticity theory which incorporates the influence of 3D non-uniform warping deformation. The theory is valid for prismatic beams undergoing small and linear strains at the beam sectional level. The equations of the sectional warping displacements are derived from the energy principle valid for static loading conditions. Using the known warpings, the structural flexibility or stiffness constants are determined. The derivations of the shear center (SC) and tension center (TC) offsets are established using an extended Trefftz' definition for anisotropic beams (Ref. 22). Using the prescribed assumptions, the variation of the beam strain energy at the sectional level can lead to the following relation:

(1) $$\delta U_S = \begin{Bmatrix} \delta\Lambda' \\ \delta\Lambda \\ \delta\Gamma \end{Bmatrix}^T \begin{bmatrix} A & E & G \\ E^T & H & Q \\ G^T & Q^T & R \end{bmatrix} \begin{Bmatrix} \Lambda' \\ \Lambda \\ \Gamma \end{Bmatrix}$$

where Λ is the nodal warping displacements and Γ denotes the beam strain measures as defined by,

(2) $$\mathbf{\Gamma} = \lfloor u_{,x} \quad v_{,x} - \beta_z \quad w_{,x} + \beta_y \quad \phi_{,x} \quad \beta_{y,x} \quad \beta_{z,x} \quad \phi_{,xx} \rfloor^{\mathrm{T}}$$

where u, v, w are the translational displacements along x, y, z directions, respectively, with x directs the beam axis, ϕ is the sectional twist angle about x axis, β_y, β_z are the section rotations, respectively, and $(\,)_{,x}$ denotes the partial differentiation with respect to x. The matrices *A*, *E*, *G*, *H*, *Q*, and *R* appeared in Eq. (1) describe the effects related with the geometric and material couplings of the beam section. The principle of virtual work is applied to derive the governing equations of the beam. The resulting (7×7) stiffness matrix can be written in a form as:

(3) $$\mathbf{K} = \begin{bmatrix} \mathbf{K}_T & \mathbf{K}_{TW} \\ \mathbf{K}_{TW}^T & \mathbf{K}_W \end{bmatrix}$$

where $\mathbf{K}_T$ represents a (6×6) Timoshenko-like stiffness matrix, $\mathbf{K}_W$ is the direct warping stiffness matrix due to nonuniform torsion, and $\mathbf{K}_{TW}$ describes a coupling between generalized Timoshenko and section warping, respectively. As a generic beam code, the sectional properties are provided at user defined axes (e.g., shear center). The recovery of sectional strains and stresses under various loading conditions is also incorporated in the analysis. For convenience of modeling, several finite elements are available such as 3- and 6-noded triangular elements, and 4- and 8-noded quadrilateral elements.

For the dynamic analysis of 1D global beam, the sectional mass and inertial properties are needed. The 3D kinetic energy is resolved to yield the sectional inertial properties. The kinetic energy of the beam is given by:

(4) $$T = \frac{1}{2}\int_l\int_A \rho \mathbf{V}^{\mathrm{T}}\mathbf{V}\,dAdx = \frac{1}{2}\int_l\int_A \rho \tilde{\mathbf{V}}^{\mathrm{T}}\mathbf{B}^{\mathrm{T}}\mathbf{B}\tilde{\mathbf{V}}\,dAdx + \frac{1}{2}\int_l\int_A \rho\left(\tilde{\mathbf{V}}^{\mathrm{T}}\mathbf{B}^{\mathrm{T}}\dot{\Psi} + \dot{\Psi}^{\mathrm{T}}\dot{\Psi}\right)dAdx$$

where ρ is the material density, $\mathbf{V}$ is the velocity vector of an arbitrary point on the cross-section, $\tilde{\mathbf{V}}$ is the vector that contains the linear and angular velocities of the reference origin of the cross-section, $\mathbf{B}$ is a permutation matrix, Ψ is the sectional warping vector, A is the area of the cross-section, and l is the length of the beam, respectively. Each $\tilde{\mathbf{V}}$, $\mathbf{B}$, and Ψ is defined as follows:

(5) $$\tilde{\mathbf{V}} = \lfloor V_x \quad V_y \quad V_z \quad \omega_x \quad \omega_y \quad \omega_z \rfloor^{\mathrm{T}}$$
$$\mathbf{B} = \begin{bmatrix} 1 & 0 & 0 & 0 & z & -y \\ 0 & 1 & 0 & -z & 0 & 0 \\ 0 & 0 & 1 & y & 0 & 0 \end{bmatrix}$$
$$\Psi = \lfloor \psi_x \quad \psi_y \quad \psi_z \rfloor^{\mathrm{T}}$$

where V_x, V_y, V_z are the velocity components, and $\omega_x, \omega_y, \omega_z$ are the angular velocities of the reference origin, ψ_x is the out-of-plane warping, and ψ_y, ψ_z are the in-plane warpings along y and z axes, respectively. Neglecting the sectional warpings, the kinetic energy T_{1D} per unit length of the beam can be expressed as:

(6) $$T_{1D} = \frac{1}{2}\tilde{\mathbf{V}}^{\mathrm{T}}\left(\int_A \rho \mathbf{B}^{\mathrm{T}}\mathbf{B}\,dA\right)\tilde{\mathbf{V}} = \frac{1}{2}\tilde{\mathbf{V}}^{\mathrm{T}}\mathbf{M}\tilde{\mathbf{V}}$$

where $\mathbf{M}$ is a (6×6) cross-sectional inertia matrix which is given by,

(7) $$\mathbf{M} = \begin{bmatrix} m & 0 & 0 & 0 & Q_y & -Q_z \\ & m & 0 & -Q_y & 0 & 0 \\ & & m & Q_z & 0 & 0 \\ & & & I_{yy}+I_{zz} & 0 & 0 \\ & & & & I_{yy} & -I_{yz} \\ \text{Sym.} & & & & & I_{zz} \end{bmatrix}$$

where m is the mass per unit length, (y_{mc}, z_{mc}) is the location of the mass center (CG), Q_y and Q_z are the first mass moments of inertia (MoI), I_{yy} and I_{zz} are the second MoI, and I_{yz} is the product MoI, defined respectively as:

(8) $$\begin{aligned} m &= \int_A \rho dA, \quad Q_y = \int_A \rho z dA, \quad Q_z = \int_A \rho y dA \\ I_{yy} &= \int_A \rho z^2 dA, \quad I_{zz} = \int_A \rho y^2 dA, \quad I_{yz} = \int_A \rho yz dA \end{aligned}$$

2.5. Rotating Free Vibration Analysis

The governing differential equations of motion for a blade under rotation is defined using the Hamilton's energy principle (Ref. 19):

(9) $$\int_{t_1}^{t_2} \left(\delta U - \delta T\right) dt = 0$$

where t_1 and t_2 are the arbitrary instants of time, and δU and δT are the first variation of the strain energy and the kinetic energy, respectively. The variation of the strain energy can be expressed using the beam force-displacement relations as:

(10) $$\delta U = \int_0^l \delta \boldsymbol{\Gamma}^{\mathrm{T}} \mathbf{K} \boldsymbol{\Gamma} dx + \int_0^l F_0 \begin{bmatrix} \delta v_{,x} \\ \delta w_{,x} \\ \delta \phi_{,x} \end{bmatrix}^{\mathrm{T}} \begin{bmatrix} 1 & 0 & 0 \\ 0 & 1 & 0 \\ 0 & 0 & k_A^2 \end{bmatrix} \begin{bmatrix} v_{,x} \\ w_{,x} \\ \phi_{,x} \end{bmatrix} dx$$

where k_A denotes the polar radius of gyration, and F_0 is the centrifugal force at a material point x as

(11) $$F_0 = \int_x^l m\Omega^2 x dx$$

The second terms in the right-hand side of Eq. (10) denote the centrifugal stiffening due to the rotation of a blade. In deriving Eq. (10), the higher-order nonlinear terms have been discarded (Ref. 20). The variation of the kinetic energy of a rotating blade is written as

(12) $$\delta T = \int_0^l \int_A \rho \delta \mathbf{V}^{\mathrm{T}} \mathbf{V} dA dx$$

where the velocity vector $\mathbf{V}$ contains the constant rotational speed component. Following the procedures in Refs. 20 and 21, one can obtain the kinetic energy variation as:

(13) $$\delta T = \int_0^l \delta \mathbf{q}^{\mathrm{T}} \mathbf{M} \ddot{\mathbf{q}} dx + \Omega^2 \int_0^l \begin{bmatrix} \delta u \\ \delta v \\ \delta \phi \end{bmatrix}^{\mathrm{T}} \begin{bmatrix} -m & 0 & 0 \\ 0 & -m & 0 \\ 0 & 0 & \underline{I_{zz} - I_{yy}} \end{bmatrix} \begin{bmatrix} u \\ v \\ \phi \end{bmatrix} dx$$

where Ω is the rotor rotational speed and the dot denotes the derivative with time. The term underscored in Eq. (13) accounts for the propeller moment, and $\mathbf{q}$ contains the 1D generalized beam displacements expressed as:

(14) $$\mathbf{q} = \lfloor u \quad v \quad w \quad \phi \quad \beta_y \quad \beta_z \rfloor^{\mathrm{T}}$$

The FE formulation is applied to describe the 1D generalized displacements of the blade. Accordingly, the beam variables ($u, v, w, \beta_y, \beta_z$) are approximated using four-node Lagrangian polynomials while the twist ϕ is expressed using a two-node Hermite shape function to secure the continuity of the rate of twist in Eq. (10). This results in 24 degrees of freedom per the element. The FE equations of motion for the blade in rotation are then expressed in the following form:

(15) $$\bar{\mathbf{M}} \ddot{\bar{\mathbf{q}}} + \bar{\mathbf{K}} \bar{\mathbf{q}} = \mathbf{0}$$

where $\bar{\mathbf{M}}$ and $\bar{\mathbf{K}}$ are the global mass and stiffness matrices of the FE system, and $\bar{\mathbf{q}}$ denotes the unknown nodal displacement vector, respectively.

3. RESULTS AND DISCUSSION

Some of the blade structural properties evaluated using the KSAC2D are presented first. A comprehensive validation on the natural vibration characteristics of the blade is then made against the detailed 3D analysis results predicted using a commercial FE analysis software and the measured data obtained in both rotating and non-rotating conditions. Finally, a sensitivity analysis is performed to examine the influence of various parameters affecting the correlation against the measured data and the vibration spectra of the blades.

3.1. Blade structural properties

Figure 8 shows the spanwise distribution of the representative blade elastic properties calculated using the general-purpose cross-sectional analysis program KSAC2D. The predictions cover the blade root, transition, airfoil (uniform), and the tip (see Figure 4). The solid rectangles indicate the predicted values at the respective blade stations (R1 to U4). Considering the uniform distribution of structural properties over the airfoil blade region, the horizontal axis scale is cut short (between 0.25R and 0.9R) for brevity. For the flap bending and torsion stiffnesses, their measured values are available (Ref. 8) and included (solid triangles) in Fig. 8 for a comparison purpose. Only the uniform portion of the blade was measured using a cantilevered condition of the blade (Ref. 8). Reasonable agreements are obtained for the flap bending (Fig. 8(a)) and torsion moments (Fig. 8(c)), as compared with the measured values. In Fig. 8, the elastic property distributions obtained for the blade arm region (inboard of the blade bolt) are also presented. As depicted in Fig. 1(b), the blade arm is composed of collocated flap/lag hinges, pitch bearing, torque tube, and pitch arm. They are mostly heavy and stiff, resulting in abrupt changes in the properties due to discrete edges of the respective metal components. The pitch bearings are installed between the inner nonrotating spindle and the external rotating (variable pitch) torque tube for accommodating the desired pitch changes. This external torque tube is directly connected to the blade bolt, so the blade loads are transmitted through the rotating torque tube, pitch bearings, non-rotating spindle, and the hub center. In this structure, there is a possibility in describing the blade load carrying through either single load path (SLP) or multiple load path (MLP). The elastic properties according to the two different load paths are available and presented together in Fig. 8. Their impact on natural vibration characteristics of the rotor will be examined in later section.

Figure 9 shows the sample results on sectional chordwise offsets for U1 section. The quarter chord (QC) position of the airfoil NACA 23012 is indicated as a reference. It is shown that, based at the QC, the SC is positioned about 4.1% chord ahead to the leading edge (LE) while TC and CG are shifted slightly toward the trailing edge. The measurement in Ref. 8 showed similar results of predicting the SC approximately at 20% chord position from the LE (5% from QC). Note that the measured SC were averaged between flap-up and flap-down bending measurements. Figure 10 shows the correlation between the predicted blade mass and the measured data. The measured blade mass is obtained by averaging between the five blades (four plus one spare blade) which include all the external equipment such as the root cable box (weighing 475 g) and the tip cap (20 g). The predicted blade mass shows an excellent agreement with the measured data. Neglecting the external attachments, the pure blade structure is estimated to be about 2.95 kg equipped with instrumented sensors, actuators, and their associated cables inside the structure. This good correlation of the blade mass implicates the suitability of the present cross-sectional analysis results that can readily be applied to exploit the natural vibration characteristics of STAR II blades.

3.2. Validation of Results

The present predictions obtained using the KSAC2D are validated first against the detailed 3D FE analysis results by MSC.NASTRAN. To this purpose, the cross-sectional FE model of U1 is extruded into a length of 2 m to create a 3D blade structure. Figure 11 shows the 3D FE model constructed for the blade. About 4,596,000 elements are formed using a 8-noded solid brick element CHEX8. The centroidal offsets (SC, TC) are determined using the cantilevered condition of the blade. Figure 12 depicts the schematic of the way how to find the SC at the section. The SC is defined as a point in a section that leads to bending without twist deformation. The loading end at the tip is simulated using the kinematic coupling RBE2 option. A unit vertical shear force is applied at an arbitrary point near the LE (point 1) or the trailing edge (point 2) while measuring the twist deformation at each load application. The shear center is found connecting the line of twist deformation between the two points. In addition, the TC is defined as a point in the section that leads to axial deformation without inducing any bending motion. The TC is found in a similar way (Fig. 12) using the 3D blade model. Figure 13 shows the comparison of the sectional offsets predicted using the present KSAC2D (blue bar) and MSC.NASTRAN 3D (white bar) analyses. The correlation of the sectional offsets is shown to be excellent for both TC and SC positions. The free vibration analysis of the uniform blade (section U1) with a clamp at the station of 275 mm is conducted next (Fig. 11). The comparison of predicted frequencies is presented in Fig. 14 for the computed eight frequency results of the lowest flap (nF), lag (nL), and torsion (nT) modes (n: mode number). The correlation between the two predictions appears excellent except the second lag (2L) mode indicating less satisfactory agreements. The close coupling of 2L and 2T modes may cause the discrepancies between the 2D and 3D predictions.

The measured frequencies of a vertically mounted STAR blade with clamped root (Fig. 2(a)) are correlated with the predicted results. The clamped condition enables focusing only the elastic part of the blade dynamic behavior and thus useful to confirm the validity of the pure structural model. Figure 15 compares the predicted natural frequencies with the measured data for flap and torsion modes. Both predictions by CAMRAD II and KSAC2D are presented for relative comparison, and good matches are observed among the predicted results. The agreements are generally good against the measured data for low flap and torsion modes and become deteriorated at higher modes. It should be noted that the STAR II blade allows very limited space (less than 35 mm) to clamp at the root, since the cable terminal box is positioned near the blade bolt (see Fig. 1). An insufficient clamping at the root plays some roles for the gap. Considering the correlation results of the clamped blade cases, the estimated blade structural properties appear realistic and relevant for stepping into the next stage of the analysis.

Next, the updated blade properties are fed into a rotorcraft comprehensive aeromechanics analysis program CAMRAD II (Ref. 12) to obtain the natural vibration modes of the blades in a rig condition (Fig. 3). Figure 16 shows the structural FE model and the aerodynamic panels employed for the aeromechanics analysis, respectively. The blade is discretized as 17 FEs and 19 aerodynamic panels along the length. The aerodynamic model includes the blade root shank which contributes to generate a drag without producing any lift. The coefficient of drag (c_d) is approximated to be 0.4 based on CFD (Computational Fluid Dynamics) computations. The FE model incorporates the blade arm region (inboard of the blade bolt). Most of the blade arm parts are modeled as elastic elements reflecting the distribution of sectional properties as depicted in Figure 8, except the innermost part connected between the blade hinges and the rotor hub center. The latter is considered very stiff and modeled as a rigid element in CAMRAD II. Figure 17 shows the correlation of the present predictions with the measured data. Reasonable agreements are seen to be obtained for the blade in rigged condition. The present results consist of the predictions with or without the external attachments (e.g., root cable box and tip cap). As depicted in Fig. 10, the mass of the blade attachments amounts about 0.495 kg. The influence of neglecting the attachments is substantial and the maximum deviation is about 6% based on the measured values.

Finally, the free vibrating responses of the STAR II blades in rotating condition are considered. Figure 18 shows the comparison of the predicted rotating natural frequencies against the measured data, depicted as a function of the rotor rotational speeds. The present results are obtained using a collective pitch setting of 5° either in vacuum (dotted red lines) or in air (continuous blue lines) condition. The frequencies are non-dimensionalized by the rotor nominal speed Ω_0 (see Table 1) and each blade mode is identified by the modal vector while considering their orthogonality feature. The frequency ranges covering up to 12 /rev (per revolution) are presented in the plot. The measured frequencies identified by their respective modes are indicated in solid circular symbols, while the predicted results are marked as lines with different colors and styles. As can be seen in Fig. 18, the influence of air is seen to be negligible except near or above the nominal rotor speed and in cases where the bending and torsion modes are highly coupled. The predicted frequencies in air generally improve the correlation with the measured data, particularly the first torsion mode. The second lag mode indicates good correlation with the measured data; however, the flap and torsion modes show good to poor agreements over the rotor speed ranges. Specifically, the second torsion mode (2T) is significantly underestimated with the present analysis. As will be shown later, the underprediction is closely related with the use of a soft pitch bearing stiffness. Based on the observations in Fig. 18, the effect of air is incorporated throughout the following studies.

Figure 19 shows the influence of load paths (SLP vs MLP) on rotating natural frequencies of the blade. To address the respective load cases, each property distribution shown in Fig. 8 which covers between the blade bolt and the flap/lag hinges is separately fed into the rotating dynamics analysis. In the MLP case, the blade loads are carried through the rotating (pitch varying) torque tube (torsion) and the non-rotating spindle (bending) in a separate mechanism. The internal nonrotating spindle is assumed to be connected to the rotating part at the blade attachment point. It is observed that the frequency responses appear virtually unaffected by the different mechanisms in load paths. It is assumed in the present analysis that there is no engagement with the snubber system connecting the rotating and non-rotating parts. The identification of the snubber property may result in more enhanced predictions while addressing the influence of the blade load paths correctly.

3.3. Parametric Investigation

In this section, several parameter changes are investigated to enhance further the quality of the predictions. The sensitivity parameters include the pitch bearing stiffnesses, anisotropic couplings of composites, and flap bending stiffnesses. Figure 20 shows the influence of varying the pitch bearing stiffnesses (K_θ) on free vibration responses of the rotor. The pitch bearing stiffness is measured using an aluminum lever arm (925 mm long) mounted to the blade control linkage resulting in an amount of about 3,945.8 Nm/rad. The K_θ is varied to 10,000 and 20,000 Nm/rad, respectively, to study its sensitivity on the natural vibrational characteristics of the blades. The resulting frequencies are presented in solid continuous lines for 20,000 and dashed lines for 10,000, respectively, as compared with the baseline cases (dotted lines). It is indicated that the increased K_θ improves the correlation with the measured second torsion (2T) significantly, while the first torsion remained nearly unchanged. The reason of significant underestimation of 2T mode with the measured pitch bearing stiffness is unclear at this moment and further study is needed before the final spring constant is determined.

For STAR II blades, the spar structure is composed of repeated symmetric boards (laminates) of 16 layers of CFRP composites while the skin consists of ∓45° GFRP (Glass Fiber Reinforced Plastic) layups. The composite layups show quasi-isotropic (spar) or balanced (skin) layer patterns to avoid serious elastic couplings of composites. Due to the geometrically-unsymmetric nature of the blade profile, the composites essentially lead to nonvanishing couplings. Table 2 shows the fully populated (6×6) cross-sectional constants obtained for U1 section. Each of the numeric numbers corresponds to: 1 extension; 2, 3 transverse shears; 4 torsion; and 5, 6 bendings. Though not prominent as compared with their diagonal counterparts, the off-diagonal stiffnesses appear non-negligible. In Figure 21, the influence of non-zero stiffness constants of composites on rotating natural frequencies is examined. Results with fully populated stiffnesses (Table 2) are compared with those neglecting the off-diagonal terms. The effects are seen to be substantial only for the second flap (2F) and the first torsion (1T) modes where they are highly coupled. The bending-torsion coupling induced due to the symmetric layups of composites is the possible source of the coupled behavior of the blade. It is remarked that the introduction of coupling terms matches better with the measured torsion (1T) mode, especially around the rotor nominal speed. In general, however, the influence of including the elastic couplings is negligible over the range of the rotor rotational speeds. The rest of the studies is thus obtained with the neglect of the elastic couplings for simplicity of the analysis.

Despite the extensive parameter studies, it is still observed that the predicted flap mode frequencies indicate significant deviations with the measured data. The rotating free vibration analysis is performed using the pitch bearing stiffness of 20,000 Nm/rad while the flap bending stiffnesses are decreased by 10% and 20%, respectively, based on the reference value. Figure 22 shows the comparison results: the dashed lines and the solid continuous lines denote the results with 10% and 20% reductions in flap bending stiffnesses, respectively. It is indicated that the decreased flap bending stiffness by 20% improves the correlation substantially with the measured data for all over rotational speed domain. The reason of requiring large reductions in the flap bending needs further investigation. The possible sources may include the reduced fiber volume fraction during the manufacturing stage of the blade, uncertainties in the material compositions, neglect of the pressure sensor bays in the structural FE model, and so forth.

4. CONCLUSIONS

In this work, the structural properties of STAR II blades were evaluated combining X-ray CT scan images and the cross-sectional analysis system. The construction details of interior structures as well as the manufacturing imperfections of the blade were essentially incorporated in the FE analysis model. The measured vibrational data were exploited to examine the soundness of the predicted elastic properties of the blade and the sensitivity of various modeling parameters of the rotor. The following conclusions were drawn from the investigation:

1. Digitally replicated analytical models for STAR II blades were shown to reflect the real fabricated

blades exactly as they were laid, particularly in terms of positioning each sensor cable distributed across the section while implementing the manufacturing imperfections.

2. The mass of the blade including all external equipment was estimated to be about 3.442 kg, resulting in an excellent agreement with the mean of the measured mass of the blades. This agreement ensured the soundness of the present FE structural analysis model.

3. The comparison of section offsets and non-rotating frequencies for clamped blades demonstrated excellent correlations with detailed 3D FE results. The measured blade frequencies in rigged condition showed good agreements for low bending and torsion modes, with the gaps increased at higher modes. An insufficient clamping at the blade root attributed to a possible source of the discrepancy.

4. The parameter study conducted for rotating blades demonstrated the impact of various factors affecting the prediction capability. The inclusion of air in the structural dynamics analysis showed negligible influence except near a curve veering region between the first torsion and the second bending modes. Similar observations were made with the non-zero elastic couplings induced due to the bending-torsion coupled layups of composites. Both led to more improved correlations with the measured data.

5. Adjusting the pitch bearing stiffness from the baseline value (3,945 Nm/rad) to 20,000 Nm/rad revealed that the predicted second torsion mode matched well with the measured data, with nearly negligible influence on the first torsion mode. In addition, a reduced flap bending stiffness by 20% demonstrated excellent agreements with the measured frequency results all over the rotor speed domain. A careful investigation was suggested to perform before the corresponding final values were determined.

Author contact:

Se Hoon Chang pattern@konkuk.ac.kr

Seong Hyun Hong shsky0721@konkuk.ac.kr

Sung Nam Jung snjung@konkuk.ac.kr

Do-Hyung Kim dhkim@kari.re.kr

Franziska Becker Franziska.Becker@dlr.de

Steffen Kalow Steffen.Kalow@dlr.de

Rinaldo Steininger 2238057s@student.gla.ac.uk

5. ACKNOWLEDGMENTS

The authors thank STAR test team for the data. This work was supported by the National Research Foundation of Korea (NRF) grant funded by the Korean government (MSIT) (2022R1A4A1018884). The work at KARI has been supported by the Korea Aerospace Research Institute's R&D program funded by the Korea Government (Ministry of Science and ICT), Republic of Korea (FR24C03). The authors acknowledge the contribution of Dr. Jae S. Bae for providing the theory section of KSAC2D.

6. REFERENCES

1. Chopra, I., “Status of Application of Smart Structures Technology to Rotorcraft Systems Piezoceramic Elements,” *Journal of the American Helicopter Society*, Vol. 45, (4), Oct. 2000, pp. 228-252.
2. Chen, P. C., and Chopra, I., “Induced Strain Actuation of Composite Beams and Rotor Blades with Embedded Piezoceramic Elements,” *Smart Materials and Structures*, Vol. 5, 1996, pp. 35-48.
3. Cesnik, C. E. S., Shin, S. J., Wilkie, W. K., Wilbur, M. L., and Mirick, P. H.: “Modeling, Design, and Testing of the NASA/Army/MIT Active Twist Rotor Prototype Blade,” American Helicopter Society 55th Annual Forum Proceedings, Montréal, Canada, May 25–27, 1999.
4. Wilbur, M. L., Mirick, P. H., Yeager, Jr. W. T., Langston, C. W., Cesnik, C. E. S., and Shin, S. J.: Vibratory Loads Reduction Testing of the NASA/Army/MIT Active Twist Rotor, *Journal of the American Helicopter Society*, 47, (2), 2002, pp. 123–133.
5. van der Wall, B. G., Lim, J. W., Riemenschneider, J., Kalow, S., Wilke, G. A., Boyd, Jr., D., Bailly, J., Delrieux, Y., Cafarelli, I., Tanabe, Y., Sugawara, H., Jung, S. N., Hong, S. H., Kim, D. H., Kang, H. J., Barakos, G., and Steininger, R., "Smart Twisting Active Rotor (STAR) - Pre-Test Predictions," In Proceedings of the 48th European Rotorcraft Forum, Winterthur, Switzerland, Sept. 6-8, 2022.
6. Hoffmann, F., Schneider, O., van der Wall, B.G., Keimer, R., Kalow, S., Bauknecht, A., Ewers, B., Pengel, K. and Feenstra, G., “STAR Hovering Test - Proof of Functionality and Representative Results”, Paper No. 10-B, In Proceedings of the 40th European Rotorcraft Forum, Sept. 2014, pp. 1–19.
7. Kalow, S., Opitz, S., Riemenschneider, J., and Hoffmann, F., “Results of a Parametric Study to Adapt Structural Properties and Strain Distribution of Active Twist Blades”, American Helicopter

Society 72th Annual Forum Proceedings, West Palm Beach, Florida, USA, May 2016.
8. Ahn, J. H., Hwang, H. J., Jang, S. H., Jung, S. N., Kalow, S., and Keimer, R., "X-ray Computed Tomography Method for Macroscopic Structural Property Evaluation of Active Twist Composite Blades," *Aerospace*, Vol. 8, Nov. 2021.
9. Dhadwal, M. K., and Jung, S. N., “On Boundary Effects due to Nonuniform Shear and Torsional Warping for Open Section Anisotropic Beams,” *Composite Structures*, Vol. 161, 2017, pp. 350-361.
10. Dhadwal, M. K., and Jung, S. N., “Multifield Variational Sectional Analysis for Accurate Stress Computation of Multilayered Composite Beams,” *AIAA Journal*, Vol. 57, (4), 2019, pp. 1702-1714.
11. Jung, S. N., Dhadwal, M. K., Kim, Y. W., Kim, J. H., and Riemenschneider, J., “Cross-sectional Constants of Composite Blades using Computer Tomography Technique and Finite Element Analysis,” *Composite Structures*, Vol. 129, 2015, pp. 132-142.
12. Kalow, S., van de Kamp, B., Balzarek, C. and Riemenschneider, J., “Manufacturing of a Next Generation Active Twist Helicopter Rotor Blade and Experimental Results of Functionality Test”, American Helicopter Society 74th Annual Forum Proceedings, Phoenix, AZ, USA, May 2018.
13. Jung, S. N., You, Y. H., Lau, B., Johnson, W., and Lim, J. W., "Evaluation of Rotor Structural and Aerodynamic Loads Using Measured Blade Properties," *Journal of the American Helicopter Society*, Vol. 58, No. 4, Oct. 2013, pp. 1-12.
14. Jung, S. N., You, Y. H., Dhadwal, M. K., Riemenschneider, J., and Hagerty, B., “Study on Blade Property Measurement and Its Influence on Air/Structural Loads,” *AIAA Journal*, Vol. 53, No. 11, 2015, pp. 3221-3232.
15. Dhadwal, M. K., and Jung S. N., “Refined Sectional Analysis with Shear Center Prediction for Nonhomogeneous Anisotropic Beams with Nonuniform Warping,” *Meccanica*, Vol. 51, 2016, pp. 1839-1867.
16. Park, I. J., Jung, S. N., Kim, D. H., and Yun, C. Y., “General Purpose Cross-Section Analysis Program for Composite Rotor Blades,” *International Journal of Aeronautical and Space Sciences*,” Vol. 10, No. 2, 2009, pp. 77-85.
17. Lee, J. B., Kang, S. N., Lee, S. K., Im, D. K., Kang, H. J., and Lee, D. J., “Development of Improved Rotor Blade Tip Shape using Multidisciplinary Design Analysis and Optimization,” In Proceedings of the 44th European Rotorcraft Forum, Delft, The Netherlands, 19-20 Sept. 2018.
18. Pilkey, W. D., Analysis and Design of Elastic Beams, John Wiley & Sons, New York, 2002.
19. Jung, S. N., Nagaraj, V. T., and Chopra, I., “Refined Structural Dynamics Model for Composite Rotor Blades,” *AIAA Journal*, Vol. 39, No. 2, 2001, pp. 339-348.
20. Hodges, D. H., and Dowell, E. H., “Nonlinear Equations of Motion for the Elastic Bending and Torsion of Twisted Nonuniform Rotor Blades,” NASA TN D-7818, 1974.
21. Jung, S. N., and Kim, D. J., “Aeroelastic Response of Composite Rotor Blades Considering Transverse Shear and Structural Damping,” *AIAA Journal*, Vol. 32, No. 4, 1994, pp. 820-829.
22. Johnson, W., CAMRAD II: Comprehensive Analytical Model of Rotorcraft Aerodynamics and Dynamics. Johnson Aeronautics, Palo Alto, CA, 1992.

Table 1: General properties of STAR II rotor blades.

Properties	Values
Rotor type	Articulated
Number of blades N_b	4
Radius R	2 m
Chord length c	0.121 m
Rotor solidity σ	0.077
Airfoil	NACA 23012m
Nominal rotor speed Ω_0	1041 rpm
Pitch bearing stiffness K_θ	3,945.8 N·m/rad
Pitch bearing location	0.1345 m
Flap/lag hinge location	0.075 m
Lag hinge stiffness	3,013 N·m/rad
Lag damping	22.3 N·m·sec/rad

Table 2: (6×6) stiffness constants computed based at the elastic axis for U1 section.

	1^{a}	2^{b}	3^{c}	4^{d}	5^{e}	6^{f}
1	2.606E+07 (N)	6.158E+02 (N)	3.687E+03 (N)	-1.601E+03 (N·m)	-1.375E+04 (N·m)	-2.044E+05 (N·m)
2		1.352E+06 (N)	-3.788E+03 (N)	-8.259E-01 (N·m)	9.341E+02 (N·m)	5.120E+00 (N·m)
3			1.823E+05 (N)	3.665E-01 (N·m)	-7.502E+00 (N·m)	4.112E+02 (N·m)
4				1.651E+02 (N·m^2)	1.161E+00 (N·m^2)	5.126E+01 (N·m^2)
5					3.705E+02 (N·m^2)	5.775E+02 (N·m^2)
6	Sym					3.085E+04 (N·m^2)

^{a} 1-extension, ^{b,c} 2,3-chordwise, vertical shear, ^{d} 4- torsion, ^{e,f} 5,6-flap, lag bending

(a) Re-fabricated blade (epsilon)

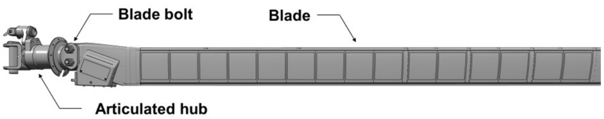

(b) Assembled view with the blade arm

Figure 1: Configuration of STAR II blades.

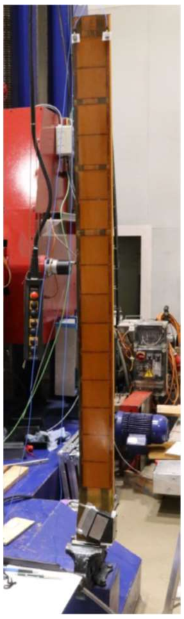

(a) Clamp condition

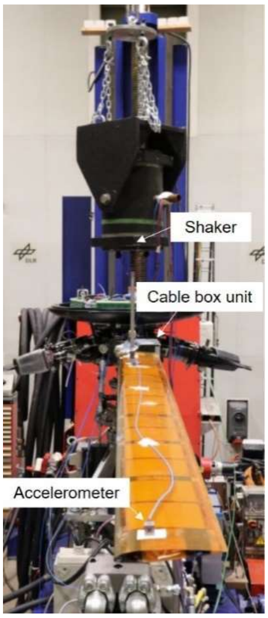

(b) Rig condition

Figure 2: Test setups for non-rotating natural modes of STAR blades (Courtesy of DLR).

Figure 3: Test setups for rotating natural frequencies of STAR blades (Courtesy of DLR).

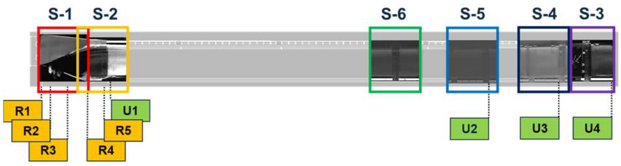

Figure 4: X-ray scan regions and the blade radial stations for sectional analysis.

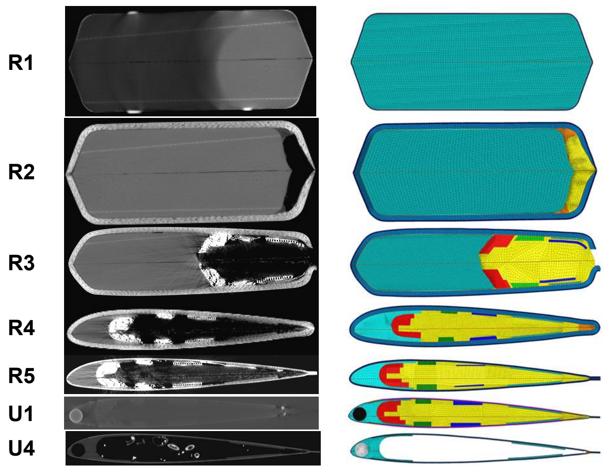

Figure 5: X-ray CT scan images and FE discretized models for the designated sections.

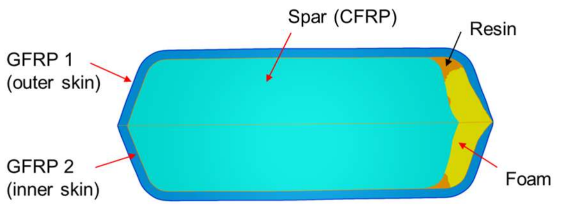

(a) Section R2

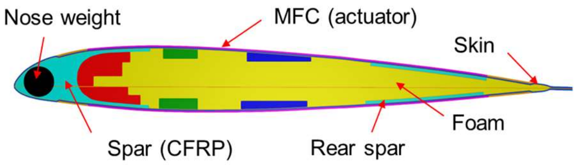

(b) Section U1

Figure 6: Section segmented images of the representative blade stations.

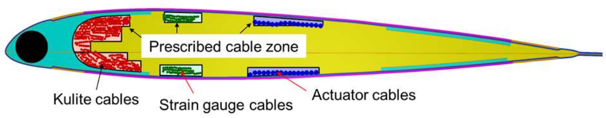

Figure 7: Partitioning of cable zones (section U1).

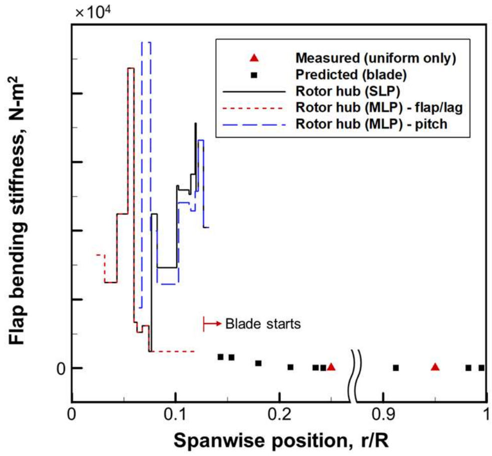

(a) Flap bending stiffness

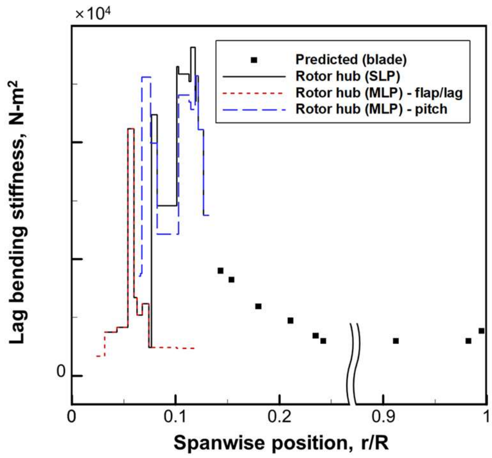

(b) Lag bending stiffness

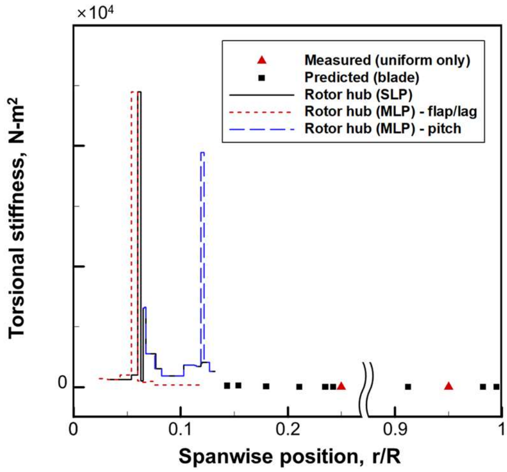

(c) Torsional stiffness

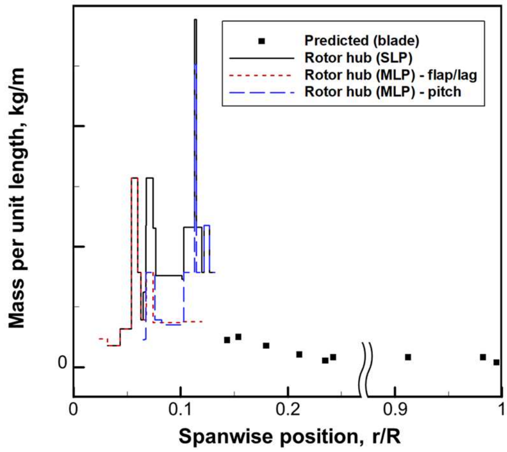

(d) Mass per unit length

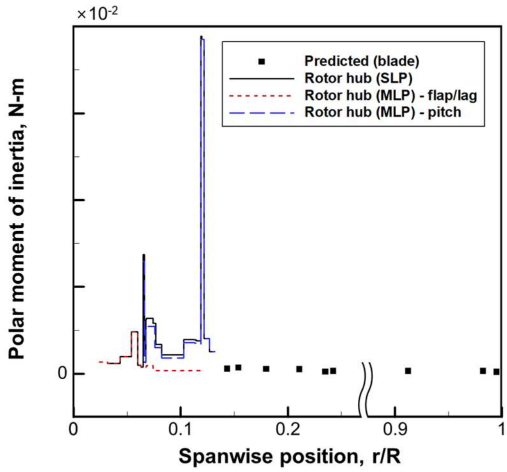

(e) Polar mass moment of inertia

Figure 8: Distribution of elastic properties for rotor hub (blade arm) and blade regions.

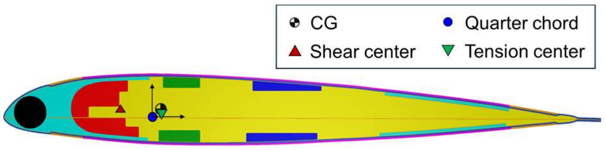

Figure 9: Computed centroidal offsets for U1 section (0.2425R).

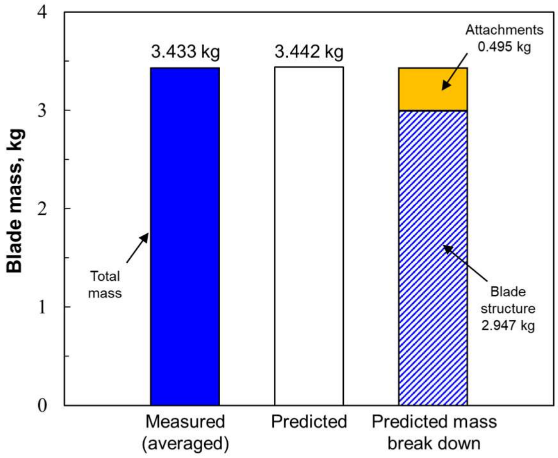

Figure 10: Comparison of predicted mass against measured data.

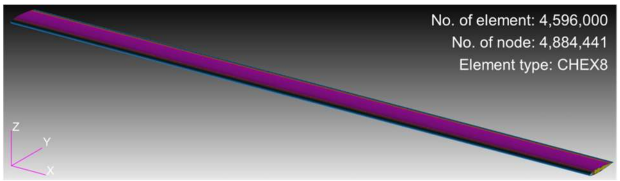

Figure 11: MSC.NASTRAN 3D FE model of uniform blade.

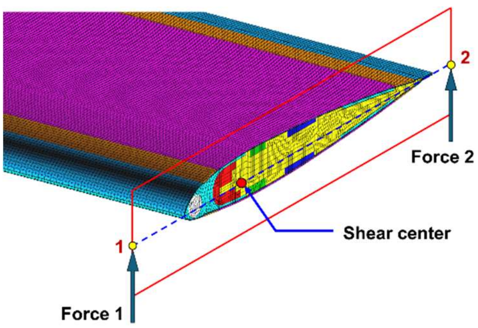

Figure 12: Application of external loads for finding the shear center in 3D FE analysis.

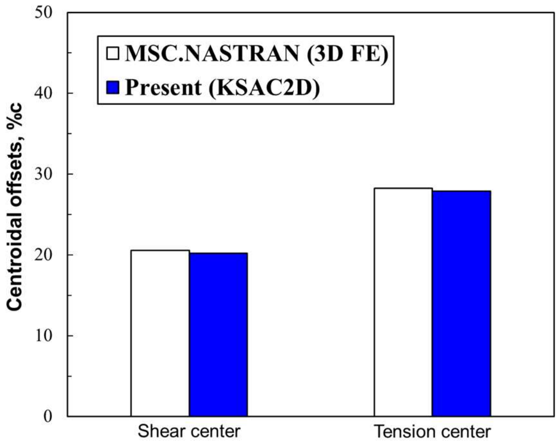

Figure 13: Comparison of predicted section offsets between MSC.NASTRAN and KSAC2D.

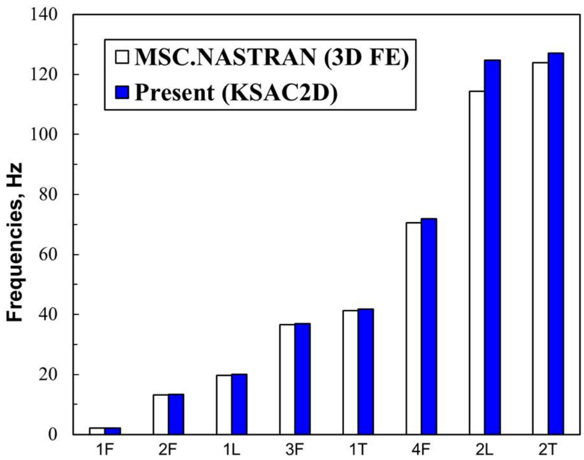

Figure 14: Comparison of natural frequencies (non-rotating) for clamped blades with uniform section only (U1).

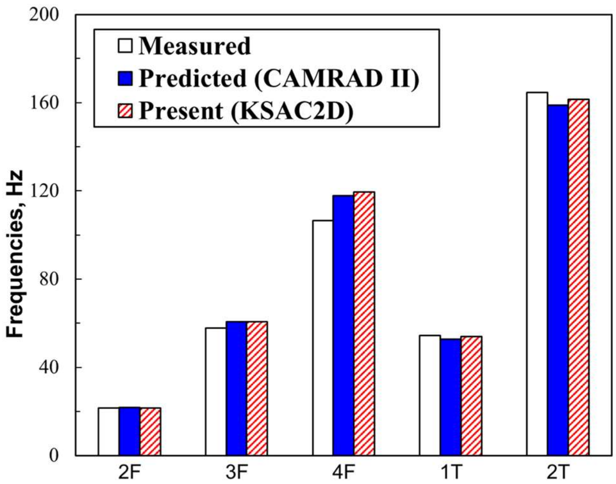

Figure 15: Comparison of natural frequencies (non-rotating) for STAR II blades in clamped condition.

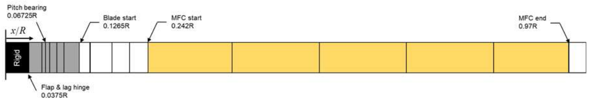

(a) Structural finite elements

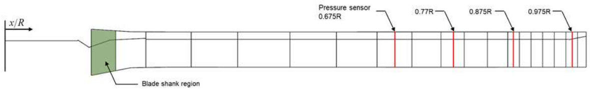

(b) Aerodynamic panels

Figure 16: Comprehensive analysis models used in CAMRAD II.

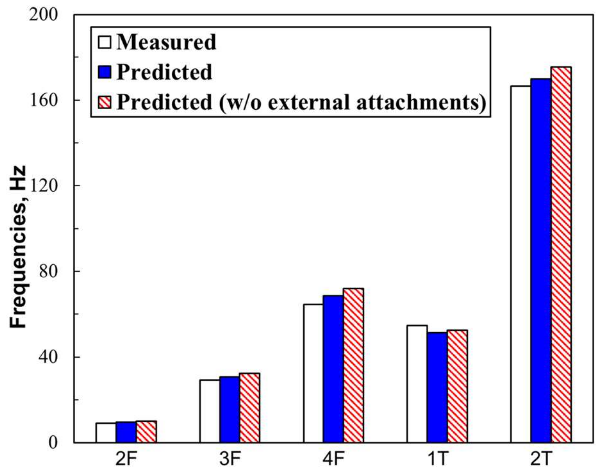

Figure 17: Comparison of natural frequencies (non-rotating) for STAR II blades in rigged condition.

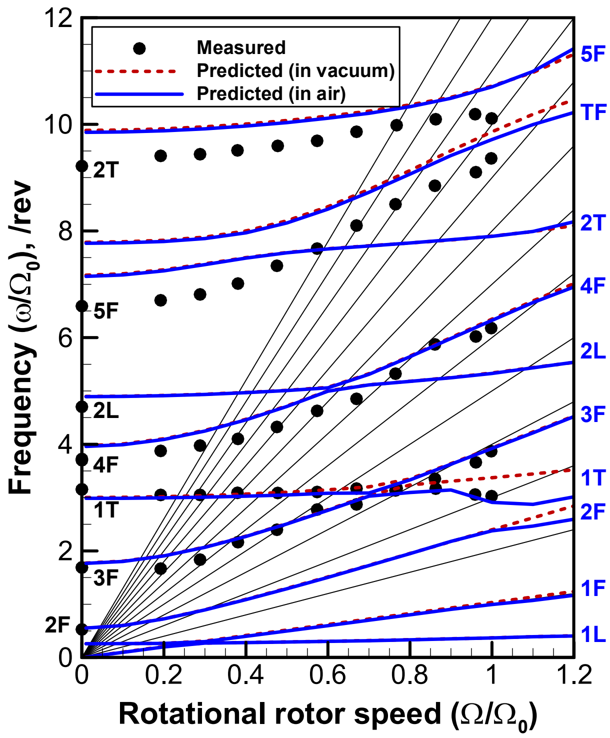

Figure 18: Comparison of rotating natural frequencies for STAR II blades.

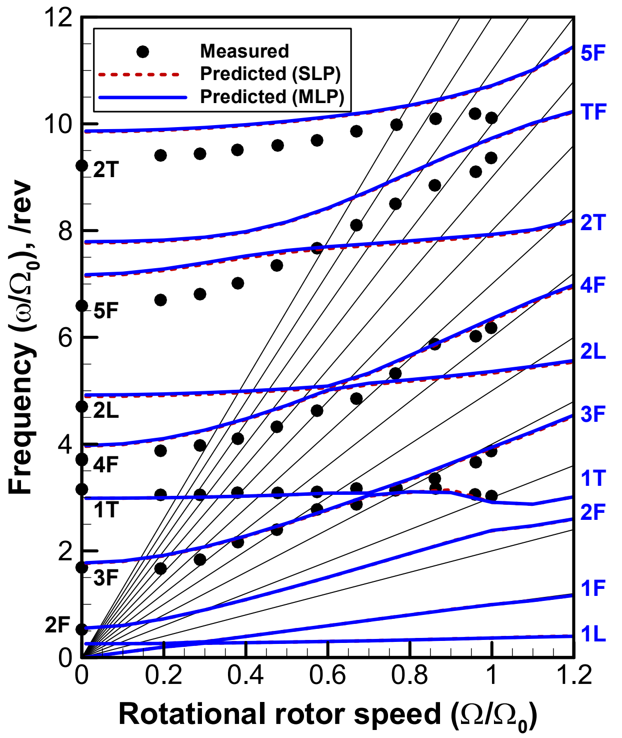

Figure 19: Effect of structural load paths on rotating natural frequencies of STAR II blades.

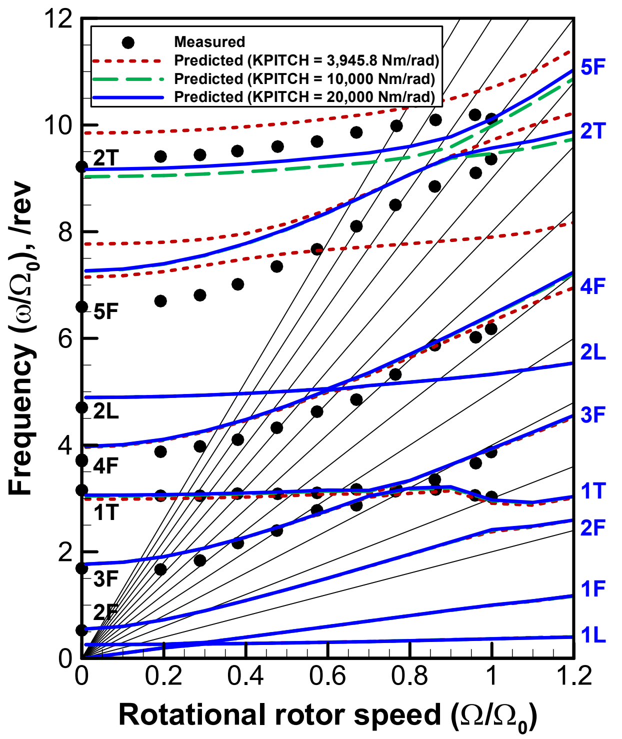

Figure 20: Effect of pitch bearing stiffnesses on rotating natural frequencies of STAR II blades.

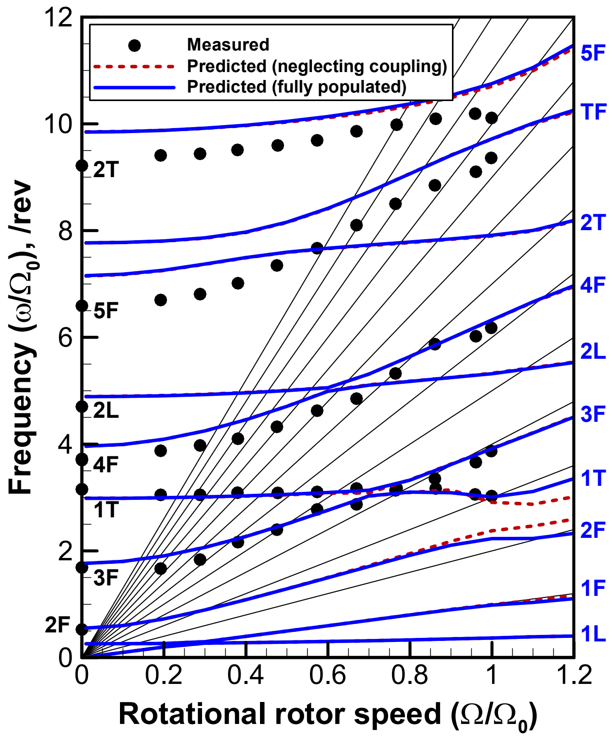

Figure 21: Effect of anisotropic couplings on rotating natural frequencies of STAR II blades.

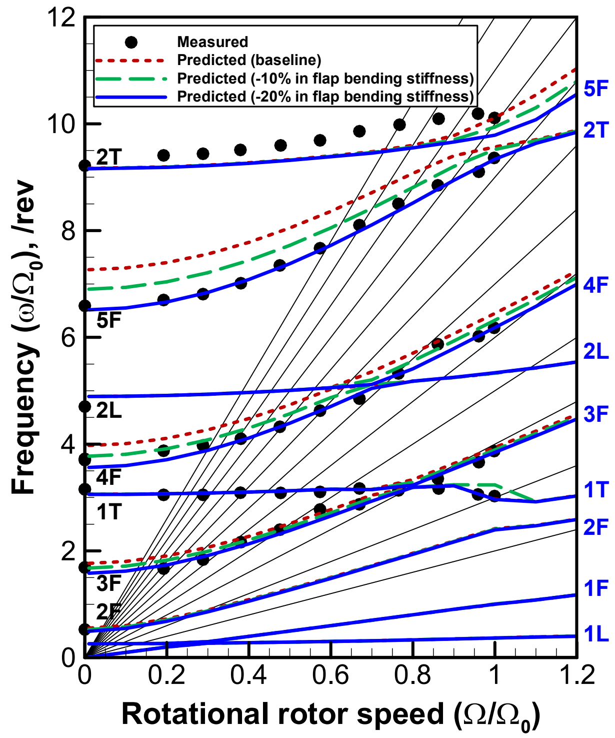

Figure 22: Effect of reduced flap bending stiffnesses on rotating natural frequencies of STAR II blades.